ADVANCES IN ATMOSPHERIC SCIENCES, 2026

• **Original Paper** •

# How Does Asymmetric Heating near the Upstream Peninsula Modulate Extreme Rainfall on the South China Coast?

Xiaoyu GAO[1], Lin SU*[2], Yu DU[2], Jinfang YIN[1], Wenxiu ZHONG[2], and Murong ZHANG[3]

[1]*State Key Laboratory of Severe Weather Meteorological Science and Technology*, *CAMS*, *Beijing* 100081, *China*

[2]*School of Atmospheric Sciences*, *Sun Yat-sen University and Southern Marine Science and Engineering Guangdong Laboratory (Zhuhai)*, *Zhuhai* 519082, *China*

[3]*State Key Laboratory of Marine Environmental Science*, *College of Ocean and Earth Sciences*, *Xiamen University*, *Xiamen* 361005, *China*

(Received 3 June 2025; revised 18 November 2025; accepted 5 January 2026)

ABSTRACT

Southerly flow within marine atmospheric boundary layer (MABL) plays an important role in the production of extreme rainfall (ER) on the South China coast (SCC). This study proposes a new perspective in that the Indochina Peninsula, which is upstream of the northern South China Sea (SCS) in the monsoon airflow, augments the southerlies in the MABL through thermodynamic forcing and thus enhances ER on the SCC. Using the 99th percentile hourly rainfall as the threshold, this study defines 337 coastal ER days in 30 early summers from 1988 to 2017. The ER days feature strong diabatic heating and downdraft-related adiabatic heating over the Indochina Peninsula, enhancing the southwestward low-level temperature gradient over the northern SCS, which is key to strengthening the southerlies within the MABL. Strong MABL southerly winds produce pronounced water vapor convergence over the SCC. Moreover, the diurnal variation in heating near the peninsula has an impact on the diurnal variation in the MABL wind velocities over the northern SCS, which is closely related to the diurnal ER cycle on the SCC. In numerical simulations of a typical heavy rainfall episode, ER on the SCC is significantly weakened by eliminating diabatic heating or terrain of the Indochina Peninsula in the sensitivity experiments. Weakened heating over the peninsula leads to weaker MABL southerlies and horizontal convergence near SCC, thus substantially inhibiting coastal convection.

**Key words:** extreme rainfall, marine atmospheric boundary layer, thermodynamic forcing, numerical simulation

**Citation:** Gao, X. Y., L. Su, Y. Du, J. F. Yin, W. X. Zhong, and M. R. Zhang, 2026: How does asymmetric heating near the upstream peninsula modulate extreme rainfall on the South China coast? *Adv. Atmos. Sci.*, https://doi.org/10.1007/s00376-026-5281-8.

**Article Highlights:**

- Asymmetric heating over the Indochina Peninsula produces a strong low-level temperature gradient over the northern SCS.
- The thermal structure enhances the southerly flow in MABL and the ER on the SCC.
- The diurnal ER cycle on SCC is modulated by the diurnal variation in heating over the Indochina Peninsula.

## 1. Introduction

Situated at the forefront of the East Asian summer monsoon's influences, South China stands out as a region characterized by the greatest rainfall amounts and the most frequent occurrences of extreme rainfall (ER) in China (Zhang et al., 2011; Luo et al., 2017). After the onset of the East Asian summer monsoon, a substantial influx of warm and moist air is transported from the tropical ocean into South China (Fig. 1), leading to a surge of rainfall. It forms the first rainy season, typically spanning from May to June, known as the early-summer rainy season in South China (Ding, 1992). In fact, 40%–60% of the annual rainfall in South China occurs in the early-summer rainy season, among which more than 50% is contributed by heavy rainfall events resulting from intricate interactions involving multiscale synoptic systems (Sun et al., 2019; Luo et al., 2020). Previous studies have categorized the early-summer ER into synoptic-forcing ER and warm-sector ER. Synoptic-forcing ER is closely associated with synoptic systems, including surface fronts, low-level wind shear, and low-level vortices (Li et al., 2020; Luo et al., 2020). By contrast, warm-sector ER occurs within a warm and humid zone with weak gradients of temperature

* Corresponding author: Lin SU
Email: sulin8@mail.sysu.edu.cn

© Institute of Atmospheric Physics/Chinese Academy of Sciences, and Science Press 2026

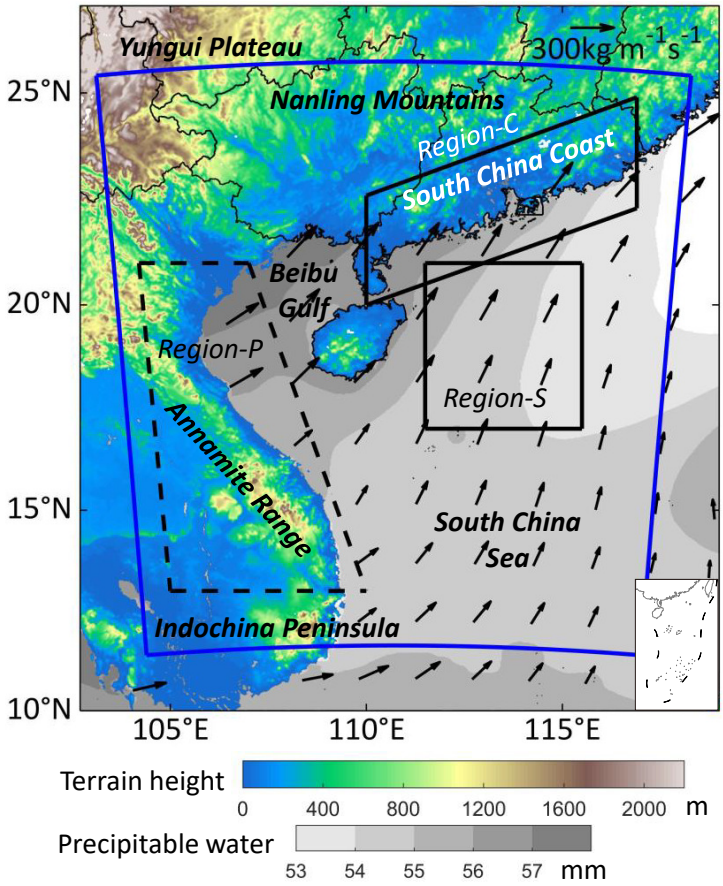



**Fig. 1.** Precipitable water (grey shadings) and columnar water vapor flux (vectors) over the sea, averaged during early summers from 1988 to 2017. Shadings over land denote the terrain height. The black-solid frames denote the two key regions, Region-C and Region-S, and the blue frame shows the domain for the WRF model. The black-dashed frame shows Region-P, where the terrain and categories of underlying surface are modified in sensitivity experiments.

and humidity, which is usually observed at the South China Coast (SCC) (Sun et al., 2019; Wu et al., 2020a). Rainfall accumulation on the SCC is mainly contributed by warm-sector ER (Luo et al., 2016; Wu et al., 2020a; Zeng and Wang, 2022). The combination of weak synoptic forcing, diverse formation mechanisms, and the characteristics of being particularly intense, abrupt, and localized, makes the prediction of ER on the SCC very challenging (Sun et al., 2019; Luo et al., 2020).

Numerous studies have revealed the close relationship between the intensity of low-level winds and ER in South China. According to the previous statistics, approximately 70% of the early-summer ER events in South China are associated with low-level jets (Li and Du, 2021). In particular, the formation of nocturnal boundary-layer jets (BLJs) with a maximum of wind velocity at ~950 hPa play a crucial role in producing heavy rainfall on the SCC (Du and Chen, 2019a; Zhang and Meng, 2019; Dong et al., 2021; Li and Du, 2021; Du et al., 2022; Du and Yi, 2025; Su et al., 2025). Moreover, ER on the SCC is characterized by a pronounced diurnal variation, manifesting a primary early-morning peak and a secondary afternoon peak (Jiang et al., 2017; Chen et al., 2018), further noting that the early-morning peak is associated with the nocturnal intensification of boundary-layer southerly flow (Chen et al., 2016; Du et al., 2020a; Su et al., 2021; Gao et al., 2022; Zhang et al., 2022; Su et al., 2023; Huang et al., 2024). Enhanced southerlies within the marine atmospheric boundary layer (MABL) produces pronounced moisture convergence and ascending motions through their interactions with local factors, such as coastal terrain (Du et al., 2020a; Zhang et al., 2022; Su et al., 2023) and land-sea breeze circulations (Chen et al., 2016; Su et al., 2021; Gao et al., 2022; Huang et al., 2024), as well as urban heat island effects (Yin et al., 2020; Sun et al., 2021), providing a conducive environment for the production of coastal ER. Numerical studies have also demonstrated the high sensitivity of ER on the SCC to the intensity of southerly flow within the MABL (Du and Chen, 2019b; Zhang and Meng, 2019; Du et al., 2020b; Wu et al., 2020b; Shen and Du, 2023). These results suggest that a precise depiction of the characteristics of MABL southerlies is critically important to the accurate prediction of heavy rainfall

on the SCC.

The formation of BLJs is associated with an enhancement in the boundary-layer winds jointly induced by thermodynamic and dynamic factors. The inertial oscillation of the boundary-layer wind is attributed to the diurnal variation in eddy viscosity (Blackadar, 1957). The baroclinic boundary layer induced by the asymmetric surface heating at sloping orography or near coastal regions also modulates the boundary-layer flows (Holton, 1967). Additionally, these boundary-layer flows can be augmented by the orographic blocking effect in mountainous regions (Li and Chen, 1998; Zhang et al., 2006; Chakraborty et al., 2009; Jiang et al., 2010; Finnigan et al., 2020). BLJs over the northern South China Sea (SCS) have been demonstrated to be attributed to a combination of the above three factors (Du et al., 2015; Du and Chen, 2019a; Tu et al., 2019; Xia et al., 2023; Du et al., 2024). Particularly, the terrain and land-sea contrast in the Annamite Range along the east coast of the Indochina Peninsula (see the terrain in Fig. 1), which is upstream of the northern SCS in the summer monsoon flow, are demonstrated in recent studies to play an important role in the formation of the BLJs in the Beibu Gulf (Kong et al., 2020; Wang et al., 2022; Du et al., 2024). The MABL winds near the leeward side of the Annamite Range undergo a nocturnal enhancement owing to the inertial oscillation. These intensified winds traverse the mountainous barrier of the Annamite Range and restrengthen through a hydraulic jump, which accelerates the downstream MABL flows through momentum advection, thereby instigating the formation the BLJs. Sensitivity experiments reveal that deactivating the surface heat flux in simulations yields the minimum occurrence frequency of BLJs over the Beibu Gulf, underscoring the critical role of the asymmetric surface heating by the Annamite Range in producing BLJs (Kong et al., 2020).

Nevertheless, the effects of the asymmetric surface heating near the Indochina Peninsula on the production of ER on the SCC and its diurnal variation remains unclear. Based upon statistical analyses and convection-permitting numerical simulations, this study attempts to address the following two questions: (1) How does the low-level thermal structure over the Indochina Peninsula enhance the southerly airflow within MABL over the northern SCS (Region-S in Fig. 1)? (2) In what ways do the enhanced MABL southerlies modulate ER on the SCC (Region-C) and its diurnal variation through thermodynamic and dynamic processes? Primarily, this study defines the coastal ER days in 30 early summer periods, and analyzes the thermodynamic forcing related to the MABL southerly flow during these days. In addition, the diurnal variation in ER and its mechanisms are discussed in two episodes. Further, the impacts of the Indochina Peninsula on the coastal ER are analyzed based on the numerical simulations of a typical case. Aside from Region-C, the Beibu Gulf coastal area (Fig. 1) is also included in the SCC, but the synoptic characteristics and mechanisms for ER in this region are quite different from Region-C, and thus, are not focused on in this study. The remainder of this paper is organized as follows. Section 2 describes the data and methods used in this study, including the model configurations. Section 3 shows the synoptic characteristics related to coastal ER. Section 4 discusses the low-level thermodynamic forcing and its impacts on the MABL wind. Section 5 examines diurnal variability, and section 6 discusses the results of numerical experiments. Finally, section 7 includes a summary and conclusion.

## 2. Data and methods

### 2.1. *Data*

This study shows the rainfall climatology in early summers (May and June) from 1988 to 2017. Hourly rainfall amounts, recorded by the national surface meteorological stations (Figs. 2a, b), are used to show the spatiotemporal distributions of coastal ER and to define ER days. The model evaluation uses observations from automatic weather stations (AWSs) and upper-air stations [see section 2 of the Electronic Supplementary Materials (ESM) ].

Two reanalysis datasets are involved in this study. The statistical analyses shown in sections 3–5 are based on the East Asia Reanalysis System (EARS) (Yin et al., 2023). This dataset has a time interval of 3 h, a horizontal resolution of 12 km × 12 km, and 74 vertical layers. The fifth generation of the European Centre for Medium-Range Weather Forecasts reanalysis (ERA5) dataset (Hersbach et al., 2020) is employed to generate the initial and lateral boundary conditions for the numerical experiments discussed in section 6. The ERA5 dataset encompasses 37 vertical layers and has a horizontal resolution of 0.25° × 0.25°.

### 2.2. *Definition of ER days*

Considering the severe disasters caused by short-duration ER events (Westra et al., 2014), this study focuses on the analysis of extreme hourly rainfall (EHR). The hourly rainfall amounts over 0.1 mm recorded by each station during the 30 early summers are sorted in ascending order, and the 99th percentile values are considered as the thresholds for EHR (Fig. 2a). As shown in Fig. 2b, the early-summer accumulated EHR exhibits three areas with values greater than 100 mm. The largest one extends along the coast from Maoming to Zhuhai, with the maximum accumulated EHR of 245.7 mm observed at Yangjiang. The other two EHR centers are located near Guangzhou and Shanwei, respectively. Note that the ER near the Beibu Gulf is also profound (Figs. 2a, b), but its mechanisms are quite different (e.g., Du et al., 2022) and thus are not the focus of this study.

Region-C includes 60 stations. If the total frequency of EHR recorded in Region-C during one day exceeds 3 (which is 5% of the station number in Region-C), this day is classified as an ER day. If more than one station recorded EHR, the total frequency is the sum of their EHR numbers, considering the heavy rainfall that either lasted for multiple hours or impacted multiple stations. Based on this definition, this study finds 337 coastal ER days, accounting for

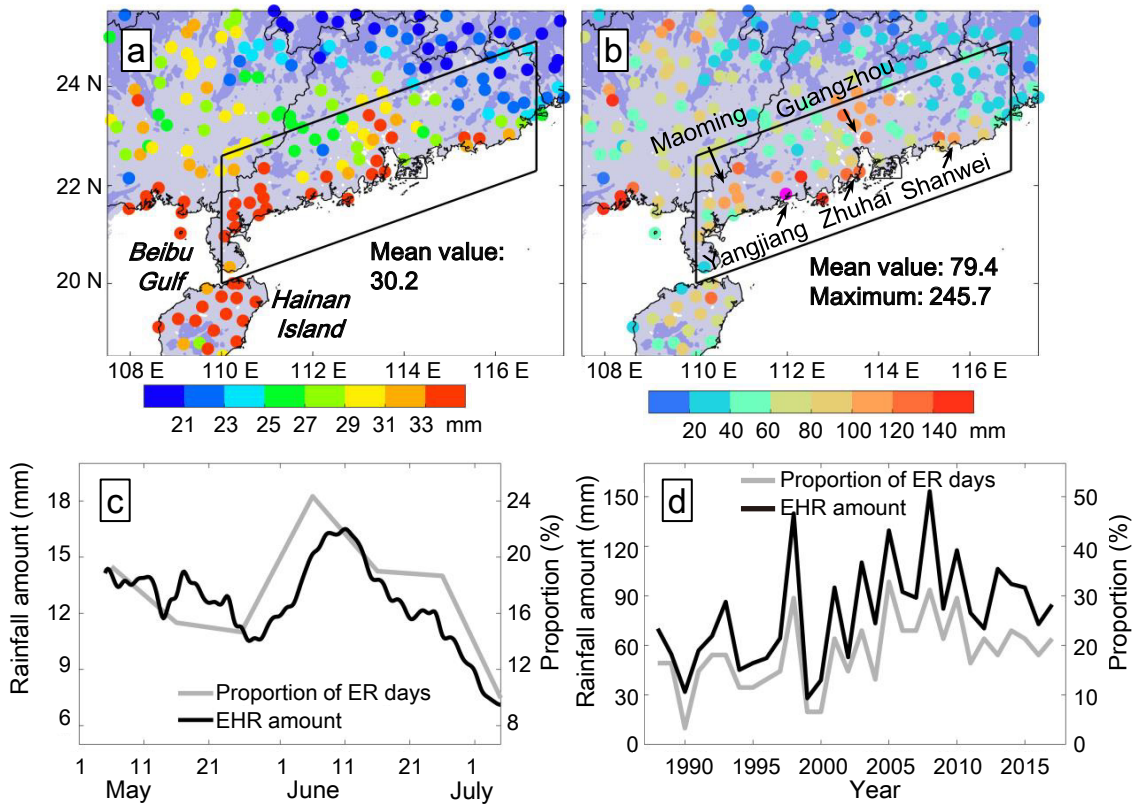



**Fig. 2.** Spatial and temporal distributions of the early-summer extreme hourly rainfall (EHR) over the SCC: (a) threshold of EHR at the 99th percentile, and (b) Seasonal accumulated EHR amount averaged during 1988–2017. The dark grey shadings in (a-b) denote topographic heights greater than 400 m, and the frames outline Region-C. (c) Time series of the 10-day accumulated EHR amount in Region-C and the proportion of ER days in ten-day intervals. (d) Interannual variations in seasonal accumulated EHR amount in Region-C and the proportion of ER days in each early-summer period.

18.4% of the total days. As shown in Figs. 2c and 2d, the ER-day proportion has a similar tendency to that of the average EHR. The 10-day EHR amount is within 10–15 mm in May, while the ER-day proportion is within 14%–20% (Fig. 2c). The most frequent onsets of the summer monsoon occurred in late May, after which the rainfall rapidly increases. The ER-day proportion reaches its peak of more than 24% in early June, while the 10-day EHR amount increases by ~5 mm. The years of 1998, 2005, 2008, and 2010 featured the most significant peaks in both the seasonal EHR amount and ER-day proportion, while the years of 1990, 1994, 1999, and 2000 consituted the low points (Fig. 2d).

### 2.3. *Force analysis*

To investigate the thermodynamic forcing in the MABL, which is closely related to the production of coastal ER, force analyses are conducted along both $x$ and $y$ directions:

$$\frac{\mathrm{d}u}{\mathrm{d}t} = -\frac{\partial \phi}{\partial x} + fv - F_x\,, \qquad (1)$$

$$\frac{\mathrm{d}v}{\mathrm{d}t} = -\frac{\partial \phi}{\partial y} - fu - F_y\,, \qquad (2)$$

I II III IV

where $u$, $v$, $\phi$, and $f$ denote the westerly component, southerly component, geopotential, and Coriolis parameter, respectively. $F_x$ and $F_y$ denote the friction forces along the $x$ and $y$ directions, which are mainly caused by the eddy viscosity. Thus, the four terms in Eqs. 1-2 denote the acceleration, geopotential gradient, Coriolis force, and friction, respectively. Following Gao et al. (2024), the geopotential gradient in MABL can be decomposed into three terms:

$$-\frac{\partial \phi}{\partial x} = -\frac{\partial \phi}{\partial x}\bigg|_{p_0} - R_d \frac{\partial \langle T_v \rangle}{\partial x} \ln\left(\frac{p_0}{p}\right) + N_x\,, \qquad (3)$$

$$-\frac{\partial \phi}{\partial y} = -\frac{\partial \phi}{\partial y}\bigg|_{p_0} - R_d \frac{\partial \langle T_v \rangle}{\partial y} \ln\left(\frac{p_0}{p}\right) + N_y\,, \qquad (4)$$

I II III IV

where term II is the geopotential gradient at $p_0$ layer in the

free atmosphere ($p_0$ is set to 700 hPa), and term III (i.e., the thermal contrast term) is the thermal wind between $p$ and $p_0$. $\langle T_v \rangle$ denotes the average virtual temperature within the two layers, and $R_d$ denotes the specific gas constant of dry air. Since the thermal wind is given according to the hydrostatic equilibrium hypothesis, a non-hydrostatic residual should be considered in the real atmosphere, which is given by term IV.

### 2.4. *Numerical experiments*

Based on numerical experiments, this study discusses the impacts of the upstream thermal structure on the production of ER on the SCC during 1–20 June 2022 (see section 1 of the ESM for an overview of this case). The simulations are conducted using the Advanced Research WRF model (Skamarock et al., 2021) version 4.3.3, and the model domain is shown in Fig. 1. The model has a horizontal resolution of 3 km × 3 km and 51 vertical layers. The 6-hourly ERA5 reanalysis data are used to generate the initial and boundary conditions. The simulation starts at 0000 UTC 27 May and stops at 0000 UTC 21 June, with the first five days (27–31 May) considered as the spin-up time. The WRF model employs the Thompson two-moment microphysics scheme (Thompson et al., 2008), the Yonsei University (YSU) planetary boundary layer scheme (Hong et al., 2006), the Unified Noah Land Surface Model (Tewari et al., 2004), and the Rapid Radiative Transfer Model for General Circulation Models longwave/shortwave radiation scheme (Iacono et al., 2008).

Three sensitivity experiments (Exp-NoDH, Exp-NoTrr, and Exp-NoDHTrr) are conducted. Their comparisons to the control experiment (denoted by Exp-Ctrl) evaluate the changes in the coastal rainfall on the SCC induced by different upstream heating. The sensitivity experiments share the same model configurations as Exp-Ctrl, but the topography and diabatic heating in the Indochina Peninsula (Region-P in Fig. 1) are modified. Exp-NoDH (where "NoDH" denotes "no diabatic heating") shuts down the latent heating of microphysical processes and sensible heating over the land surface in Region-P, while the Exp-NoTrr experiment (where "NoTrr" denotes "no terrain") decreases the terrain heights in Region-P to 0. Exp-NoDHTrr (where "NoDHTrr" denotes "no diabatic heating and terrain") conducts both the modifications in Exp-NoDH and Exp-NoTrr. It is plausible that both the diabatic and adiabatic heating in the low levels of Region-P is weakened in the sensitivity experiments.

## 3. Synoptic characteristics

The SCC meets strong MABL southerly flow from the northern SCS during ER days, which produces pronounced water vapor convergence near the coastline. As shown in Figs. 3a, the SCC lies to the east of a shallow trough of 700-hPa geopotential height (GPH) during ER days, which forces a low-level southwesterly wind. Figure 3b shows ER-day anomalies, which are the differences of variables between the ER days and their respective seasonal average. The negative GPH anomaly over South China and the positive GPH anomaly over the SCS exhibit a stronger 700-hPa geopotential gradient and higher wind velocity than the seasonal average (Fig. 3b). Note that the 700-hPa westerly component is much larger than the southerly component near the SCC, making the wind velocity almost parallel to the coastline. If the wind directions at lower layers do not change with pressure, the coastal topographic lifting should be quite weak since the convergence mainly depends on the wind component perpendicular to the coastline. However, there is significant vertical wind shear (VWS) within the 700–950-hPa layer. The southerly component increases with pressure, and its maximum occurs in the MABL, which is the key cause for coastal lifting in many ER events. The average southerly component at 950 hPa in Region-S is 6.8 m $s^{-1}$, which is two times that at 700 hPa (Fig. 3a).

As shown in Figs. 3c and 3d, the precipitable water over the sea increases rapidly from south to north, and exceeds 60 mm near the SCC, which is over 4 mm larger than the seasonal average (Fig. 1). The columnar water vapor fluxes exhibit a clear path for moisture transport from southwest (Fig. 3c). Compared to the seasonal average, the moisture transport during ER days is stronger to the south of the SCC and weaker to the north (Fig. 3d), enhancing coastal convergence of water vapor, which is conducive to the production of coastal ER. The meridional cross-section shows a thickened moist layer with raised contours of water vapor mixing ratio near the coastline, where the updraft is significant (Fig. 4a). The greatest anomaly of water vapor occurs at ~800 hPa over the SCC (Fig. 4b), which is caused by stronger convergence and updraft below this level.

The strong southerly winds in the MABL indicate a pronounced low-level baroclinicity, which is closely related to the thermal structure over SCS. The MABL over the western SCS is much warmer than the surrounding areas with a 950-hPa potential temperature that exceeded 304 K during ER days (Fig. 3a), which is ~0.8 K higher than the seasonal average (Fig. 3b). It produces a strong thermal contrast over the northern SCS, where the temperature rapidly decreases from southwest to northeast. As shown in Fig. 4c, there is a strong downdraft over the leeside of the Annamite Range, leading to strong adiabatic heating, which together with the diabatic heating over Indochina Peninsula produces the significant warm area over the western SCS (Fig. 3a). The stronger synoptic forcing during ER days further enhances the downdraft, leading to the positive anomaly of potential temperature in the MABL (Fig. 4d). On the other hand, the downdraft also decreases the moisture and produces a dry layer, enhancing the convective inhibition over Beibu Gulf, which does not affect the sea area to the east of Hainan Island (i.e., Region-S). As a result, rainfall amount near the Beibu Gulf is much lighter than that in Region-C when both areas meet BLJs (Du et al., 2022).

The characteristics of the low-level wind field and thermal structure during coastal ER days are quite robust and do not change significantly with different rainfall areas on the SCC. Based on the same definition, 387 ER days can

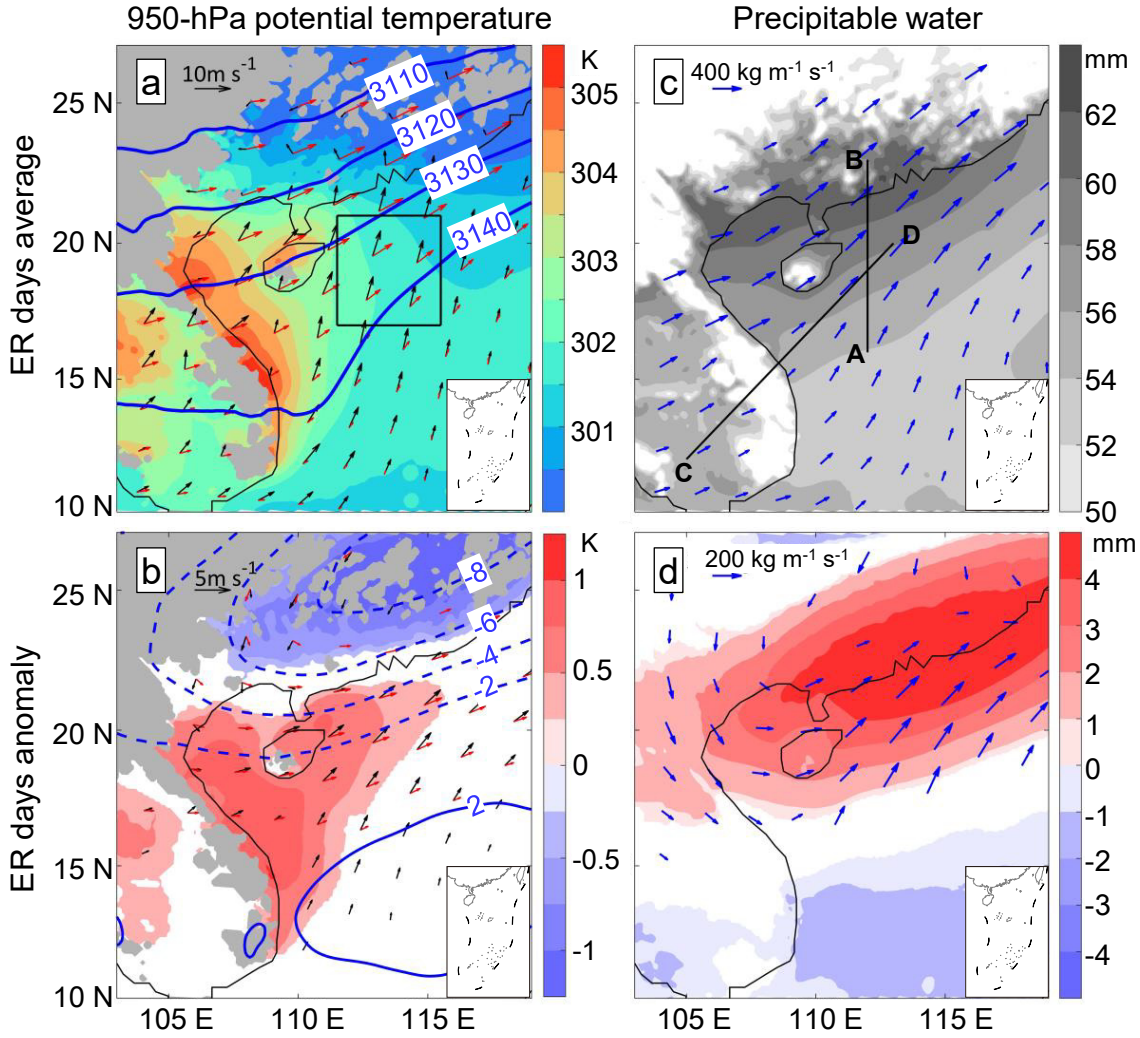



**Fig. 3.** Synoptic characteristics for ER events. The left column shows the 700-hPa geopotential height (contours; units: gpm) and wind velocities (red vectors), as well as the 950-hPa potential temperature (shadings) and wind velocities (black vectors) averaged during (a) ER days and (b) their anomalies. The right column shows the precipitable water (shadings) and columnar water vapor flux (vectors) averaged during (c) ER days and (d) their anomalies. The black frame in (a) shows the Region-S, and lines A-B and C-D in (c) show the two cross-sections cited in Fig. 4. The anomalies that are not significant at the 0.05 level are not shown in the lower row.

be found for a larger Region-C (Fig. 5a), which includes 166 stations, while 366 ER days can be found for a smaller Region-C, which includes 49 stations (Fig. 5c). The distribution of the 700-hPa geopotential height field during both episodes (Figs. 5a, c) shows a shallow trough over southwest China, which are similar to that during the original 337 ER days (Fig. 3a). The 700–950-hPa VWS over the northern SCS and 950-hPa warm tongue near the Indochina Peninsula are also similar (Figs. 5a, c and 3a), but the warm tongue during ER days for the larger Region-C is stronger (Figs. 5b, d and 3b), which leads to stronger low-level baroclinicity. In general, the synoptic characteristics in ER days are not sensitive to the scope of Region-C.

## 4. Low-level thermodynamic forcing

The asymmetric heating over the Indochina Peninsula, which results from much stronger adiabatic and diabatic heating over land than over sea, enhances the low-level thermal contrast over the northern SCS. This thermal structure produces significant VWS between the MABL and the free atmosphere. Figure 6 shows the average vertical profiles of all the terms in Eqs. 1–4 in Region-S. The zonal Coriolis force related to the southerly component results in accelerations of $1.6 \times 10^{-4}$ m s$^{-2}$ at 700 hPa increasing to $3.2 \times 10^{-4}$ m s$^{-2}$ at 950 hPa (blue line in Fig. 6a), corresponding to the low-level VWS (Fig. 3a). It is nearly balanced with the variations in zonal geopotential gradient and friction (orange and light purple lines in Fig. 6a), which is enhanced by $1.2 \times 10^{-4}$ and $0.4 \times 10^{-4}$ m s$^{-2}$ between the two layers, accounting for 74.1% and 26.9% of the increase in Coriolis force (blue line in Fig. 6a) (the extra ~1% contributes to the variations in zonal acceleration). Furthermore, the zonal thermal contrast term (purple line in Fig. 6b) contributes 120.7% to the

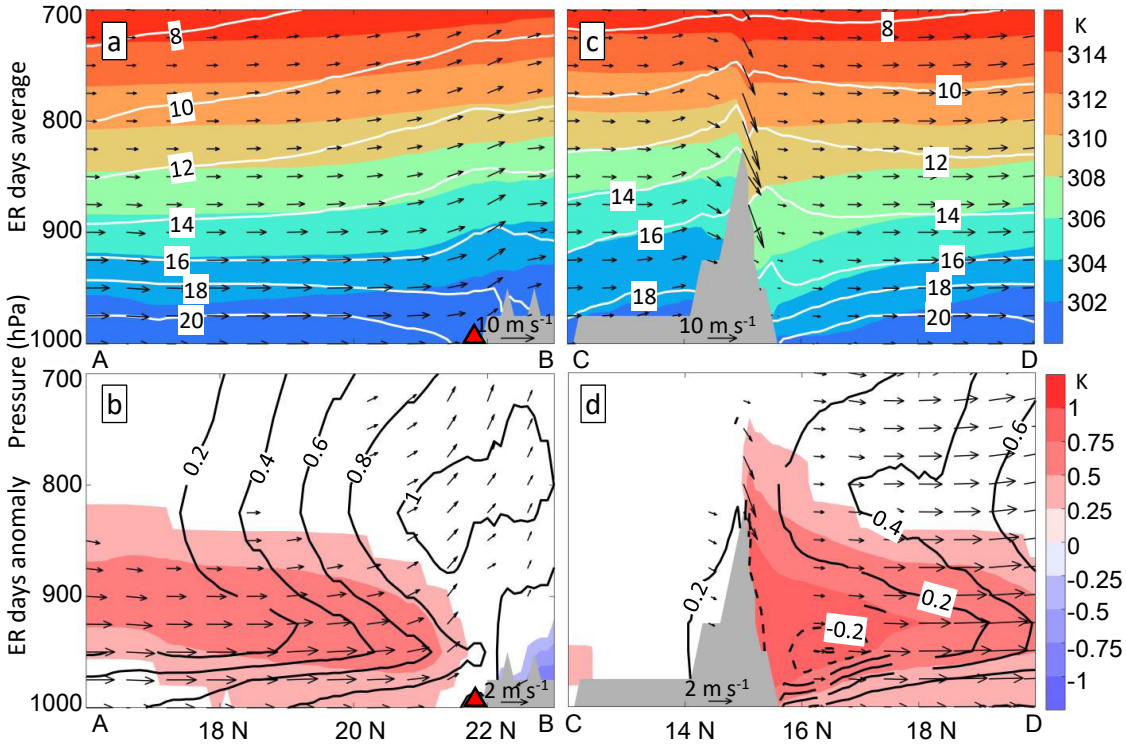



**Fig. 4.** Potential temperature (shadings), in-plane wind velocities (vectors; the vertical velocity is multiplied by 100), and water vapor mixing ratio (contours; units: g $kg^{-1}$) within the cross-sections along lines A-B (left column) and C-D (right column) in Fig. 3c. The upper row shows the values averaged during ER days, and lower row shows their anomalies. Red triangles denote the location of the coastline. Anomalies that are not significant at the 0.05 level are omitted in the lower row.

increase in the geopotential gradient at 950 hPa relative to that at 700 hPa, while the non-hydrostatic residual (pink line in Fig. 6b) offsets it by 20.7%. This indicates that the zonal thermal contrast dominates the structure of geopotential in the MABL and plays an important role in the strengthening of MABL southerly flow. Meanwhile, the meridional geopotential gradient (orange line in Fig. 6d) is $2.2 \times 10^{-4}$ m $s^{-2}$ at 700 hPa and decreases to $1.6 \times 10^{-4}$ m $s^{-2}$ at 950 hPa, which is also dominated by the thermal contrast term (purple line in Fig. 6d) with a contribution of 119.3%. The weakening of the meridional Coriolis force and corresponding westerly component of pressure gradient force (blue line in Fig. 6c) depends on both the geopotential gradient and friction (orange and light blue lines in Fig. 6c), with contributions of 46.3% and 50.2%, respectively. Note that the large meridional friction is a result of strong southerlies in the MABL, which is also related to the zonal thermal contrast.

To investigate the impacts of low-level baroclinicity and the related synoptic characteristics, ER days with strong and weak baroclinicities are selected based on the VWS within 700–950 hPa in Region-S. The daily VWS in all the ER days are sorted in ascending order, and the days with VWS weaker than the 25th percentile value are defined as weak baroclinicity days (denoted by type-WkB), while those with VWS stronger than the 75th percentile value are defined as strong baroclinicity days (denoted by type-StB). Figure 7 shows their differences in terms of low-level wind, thermal structures, and ER amounts. During type-WkB days, Region-S is to the west of the subtropical high with weak southerly flow at 700 hPa (Fig. 7a). Forced by a weak thermal contrast, the southerly component at 950 hPa is only 1.4 m $s^{-1}$ larger than that at 700 hPa. Type-StB features stronger synoptic forcing than type-WkB with a larger westerly component in Region-S (Figs. 7a, b). The stronger diabatic heating over the Indochina Peninsula and stronger downdraft-related adiabatic heating near the leeside of the Annamite Range for type-StB produces a much warmer MABL over the western SCS than type-WkB. The thermal contrast intensifies MABL southerlies, resulting in enhanced convergence near the coastal areas. The southerly component at 950 hPa is 5.3 m $s^{-1}$ larger than that at 700 hPa in Region-S (Fig. 7b). The northward moisture transport for type-StB is much stronger than type-WkB, which is mainly attributed to the increment of wind velocities below 700 hPa (Figs. 7c, d). It produces a stronger gradient of moisture over the northern SCS and more precipitable water in Region-C, and the coastal ER amount for type-StB is 37% greater. Meanwhile, one-half of the northward moisture transport is caused by the increment of wind velocities related to low-level baroclinicity, even for type-StB, and the proportion is much less during other ER days (Figs. 7c, d). This indicates that the moisture transport is mainly driven by the synoptic forcing, while the low-level baroclinicity has an auxiliary effect.

Furthermore, there is a close correlation between low-

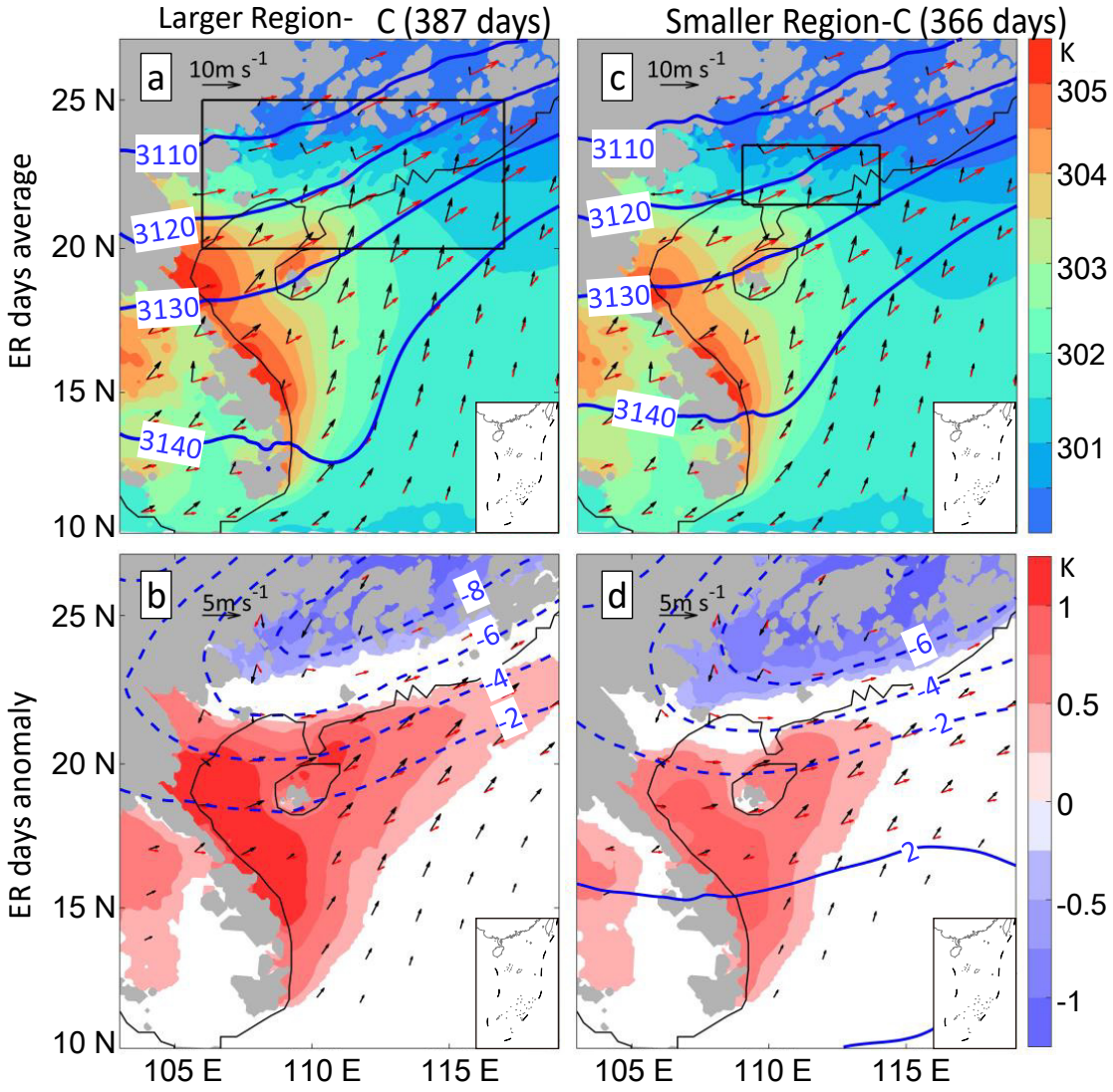



**Fig. 5.** Sensitivity of the synoptic characteristics in ER days to the scope of Region-C. (a-b) Same as in Figs. 3a-b, but for the ER days in a domain larger than Region-C (shown by the black frame). (c-d) Same as in Figs. 3a-b, but for the ER days in a domain smaller than Region-C.

level thermal contrast and VWS in Region-S (Figs. 8a, c). A warmer MABL over the western portion of Region-S is often accompanied by stronger southerlies in MABL. Meanwhile, stronger southerlies enhance the warm advection and thus the meridional thermal contrast, which exacerbates the weakening of the westerly component with height. These two mechanisms both enhance the wind component perpendicular to the coastline in MABL, which is conducive to coastal convergence and production of coastal ER. The correlation coefficient between the east-west thermal contrast and the increment of southerly component is –0.783 (Fig. 8a), and that between the north-south thermal contrast and the increment of westerly component is 0.7 (Fig. 8c). In general, a stronger 700-hPa wind often leads to stronger 950-hPa wind, with a correlation coefficient of 0.649 between the 700- and 950-hPa southerly components (Fig. 8b) and a correlation coefficient of 0.801 between 700- and 950-hPa westerly components (Fig. 8d). Nevertheless, these correlations vary with the intensity of baroclinicity. Strong low-level baroclinicity leads to intensified MABL winds, even with weak synoptic forcing in the free atmosphere. This explains the weaker correlations between 700- and 950-hPa winds for type-StB compared to type-WkB (Figs. 8b, d). Note that all correlations shown in Fig. 8 are statistically significant at the 0.05 level. The correlations related to the differences of all variables shown in Fig. 8 between type-StB and type-WkB are also statistically significant at the 0.05 level, except for that of the 700-hPa southerly component. The nature of this exception is straightforward since the 700-hPa southerly components are weak during both episodes, and the strong 950-hPa southerlies for type-StB are mainly forced by the low-level baroclinicity.

## 5. Diurnal variation

The impacts of heating near the Indochina Peninsula on

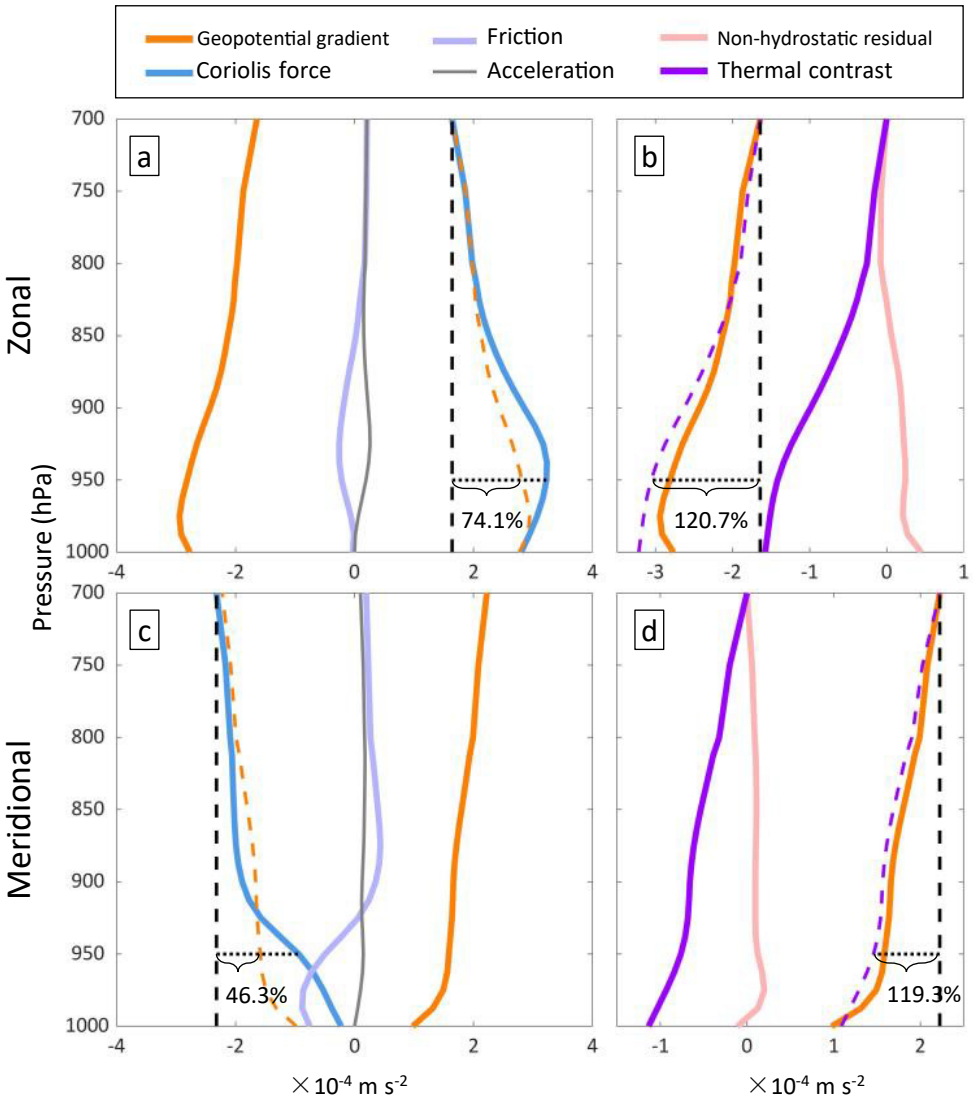



**Fig. 6.** Force analyses in Region-S during ER days. The upper row (lower row) shows all the terms in the zonal (meridional) force analysis. The black- and orange-dashed lines in the left column denote 700-hPa Coriolis force and the opposite of the geopotential gradient term, respectively, and the dotted lines denote the difference in Coriolis force between 950 and 700 hPa. The black- and purple-dashed lines in the right column denote the 700-hPa geopotential gradient and the sum of it and the thermal contrast term, respectively, while the dotted lines denote the difference in thermal contrast terms between 950 and 700 hPa.

the diurnal rainfall cycle over the SCC are discussed in this section. As shown in Fig. 9d, the coastal EHR during ER days exhibits a notable diurnal cycle, with a primary peak after sunset (at 1900 LST) and a secondary peak after midnight (at 0300 LST) (Fig. 9d), which can be attributed to the diurnal variations in offshore wind and land-sea thermal contrast.

Stronger southerlies in the MABL lead to stronger coastal convergence, increasing the probability of ER occurrence. The 950-hPa southerly wind component in Region-S varies between 6–7.5 m $s^{-1}$, which has a much larger amplitude than that above 850 hPa (Fig. 9b). It exhibits two peaks, one in the afternoon (at 1700 LST) and the other early in the morning (at 0500 LST). The increases in coastal EHR in the afternoon and at night are both accompanied by the strengthening of MABL southerly flow (Figs. 9b, d), indicating that the wind velocity in the MABL is an important factor in modulating the diurnal cycle of coastal ER. The diurnal variation in offshore wind velocity in the MABL is forced by the diurnal cycle in low-level thermal structure (e.g., Du et al., 2015). As shown in Fig. 9a, the potential temperature in Region-P shows a warmer anomaly in the afternoon than at night (Fig. 9a). Thus, the enhancement in geopotential gradient in the northern SCS is more significant during the daytime, which subsequently forces a larger southerly wind component anomaly (Fig. 9b). This causes the EHR peak in the afternoon to be more significant during ER days than in all the early summers (Fig. 9d). On the other hand, the coastal

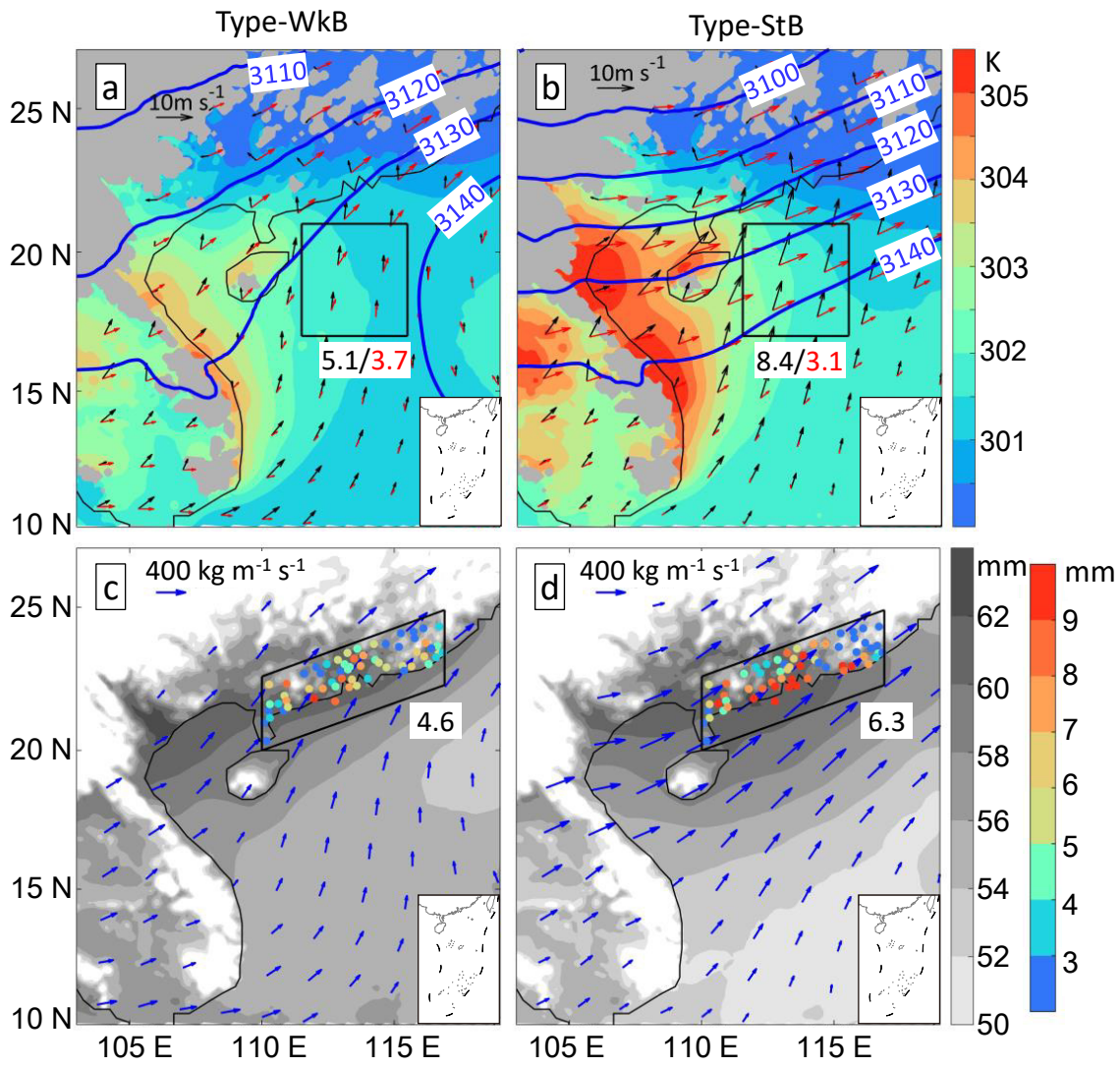



**Fig. 7.** Synoptic characteristics for two types of ER events: type-WkB (left column) and type-StB (right column). The upper row shows the 700-hPa geopotential height (contours; units: gpm) and wind velocities (red vectors), as well as the 950-hPa potential temperature (shadings) and wind velocities (black vectors). The black frames denote Region-S, and its average southerly components at 950 (700) hPa are given by the black (red) numbers. The lower row shows the average daily EHR amount (dots), precipitable water (shadings), 700–1000-hPa water vapor flux (blue vectors), and its part caused by the increment of horizontal wind below 700 hPa (yellow vectors). The black frames denote Region-C, and its average EHR amounts are given by the black numbers.

thermal contrast induces a land breeze superposed on the background southerly flow, enhancing the coastal convergence (e.g., Chen et al., 2016). The low-level air temperature onshore is usually lower than that offshore near the SCC. Hence, the nocturnal cooling over the land surface is more significant than that over sea surface, leading to a stronger land-sea thermal contrast after sunset, which can be seen in the diurnal variation in the difference of potential temperature between the northern and southern boundaries of Region-C (Fig. 9c). This also corresponds to the occurrence of the EHR peak in the early morning. The anomaly of north-south thermal contrast shows a significant enhancement in the afternoon (Fig. 9c), which is produced by the stronger offshore southerly winds during daytime (Fig. 9b) as well as a cooler land surface (since the SCC meets heavier rainfall). In summary, the warm anomaly over the Indochina Peninsula during ER days makes the enhancement of the MABL southerly flow over the northern SCS and land-sea thermal contrast near the SCC more significant during daytime, thus the EHR peak in the afternoon is more significant.

As shown in Fig. 10, the wind velocities and thermal structures during ER days with stronger low-level baroclinicity are more likely to have drastic diurnal variations. Type-StB features larger amplitudes of diurnal variations in potential temperature over Region-P (Figs. 10a, b). The mean amplitude of 950-hPa potential temperature for type-StB is 32% larger than that for type-WkB. This forces more a dramatic diurnal variation in the low-level southerly winds

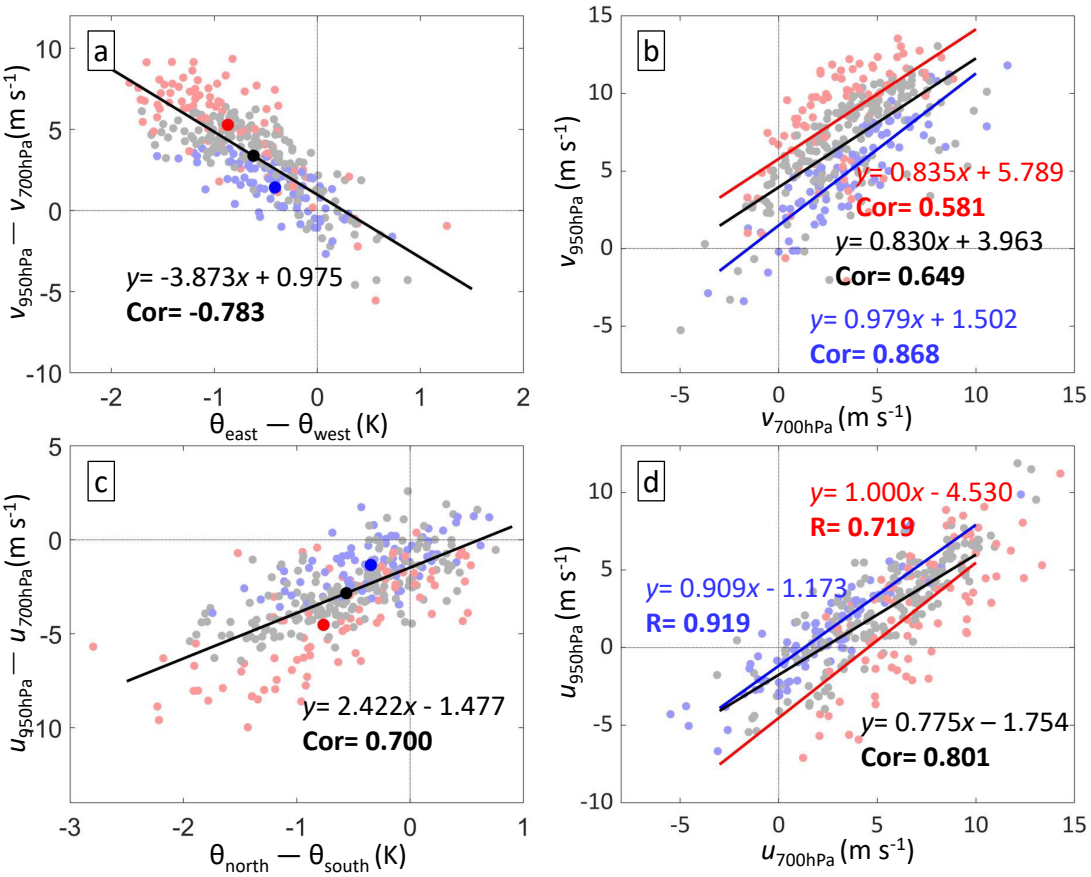



**Fig. 8.** Relationship between the 700–950-hPa VWS and thermal contrast in Region-S during ER days: (a) Distribution of the thermal contrast and the increment of southerly component in MABL, where the *x*-axis denotes the difference of MABL (900–1000 hPa) potential temperatures ($\theta$) between the east and west boundaries of Region-S, and the *y*-axis denotes the difference between 950 and 700-hPa southerly components; (b) The distribution of the 700-hPa (*x*-axis) and 850-hPa (*y*-axis) southerly components; (c) Same as in (a), but the difference of temperatures is between the northern and southern boundaries, and its wind velocity increment is for the westerly components; (d) Same as in (b), but for the westerly components. All variables are daily averages. The red (blue) dots denote the type-StB (type-WkB) days, and their linear fits are denoted by the red (blue) lines. The grey dots denote the other ER days, and the linear fits of all the ER days are denoted by the black lines.

over the northern SCS (Figs. 10c, d). The mean amplitude of the 950-hPa southerly wind component in Region-S for type-StB is 32% larger than that for type-WkB. Meanwhile, the thermal contrast in Region-C also displays a more pronounced diurnal variation for type-StB (Fig. 10e), which, together with the diurnal variations in wind velocities, amplifies the diurnal EHR cycle. The mean EHR amplitude for type-StB is 21% larger than for type-WkB.

The diurnal variation in offshore MABL temperature is usually controlled by the warm airflow from land, since the eddy heat transport is weak over the sea surface. Thus, the large amplitudes of 950-hPa potential temperature extend from the Indochina Peninsula to the northern SCS (Fig. 11). Diabatic heating over the peninsula is much stronger during type-StB days, accompanied by more drastic diurnal variation over both the peninsula and the northern SCS (Figs. 7a, b and 11a, b). The amplitudes of 950-hPa potential temperature for type-StB are ~0.5 K larger than type-WkB near the Annamite Range and ~0.2 K larger in Region-S, forcing a more pronounced diurnal variation in 950-hPa southerlies (Figs. 11a, b). On the other hand, type-StB also features stronger diabatic heating over South China (Figs. 7a, b), which leads to larger amplitudes of thermal contrast in Region-C (Fig. 10e).

## 6. Results of numerical experiments

As shown in section 2 of the ESM, the Exp-Ctrl well captures the spatiotemporal distribution of ER as well as the low-level thermal structure in Region-C during 1–20 June 2022. Thus, further analyses are based on the comparison between the Exp-Ctrl and the sensitivity experiments, which employ the same model configuration.

Both the total rainfall and EHR amounts on the SCC decrease with the modified surface heating or presence of terrain in Region-P (Fig. 12). For Exp-NoDH, EHR at the eastern center is reduced substantially (Figs. 12b, d). The western EHR center almost disappears in Exp-NoTrr and

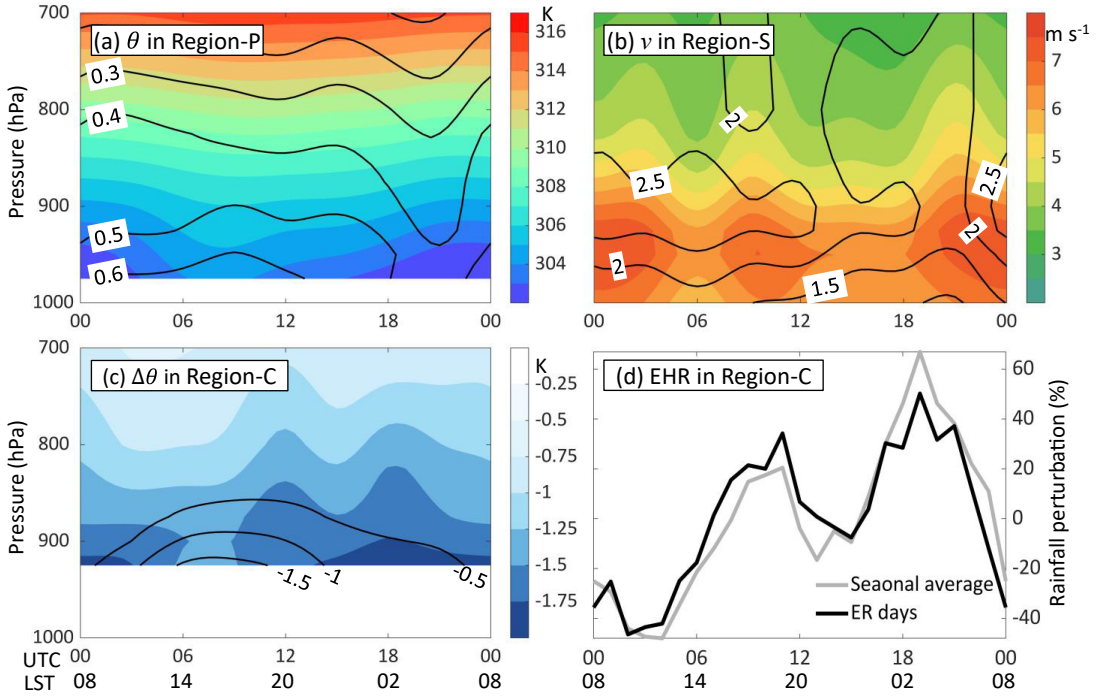



**Fig. 9.** Diurnal variations in some variables in the key regions: (a) Time–pressure distribution of potential temperature averaged in Region-P during ER days (shadings) and its anomaly (contours; units: K); (b) Same as in (a), but for the southerly component averaged in Region-S; (c) Same as in (a), but for the north-south thermal contrast (denoted by "$\Delta\theta$") in Region-C; (d) The diurnal variation (given by the perturbation relative to the daily average) in the EHR in Region-C. All anomalies shown in (a–c) are statistically significant at the 0.05 level.

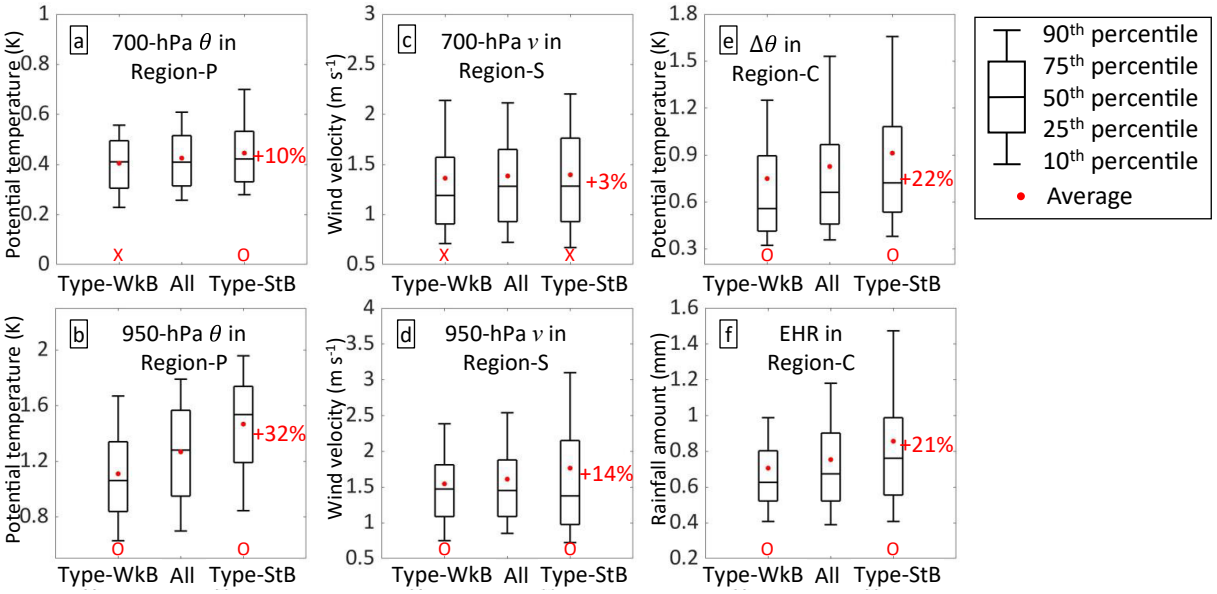



**Fig. 10.** Distributions of diurnal variation amplitudes during type-WkB, type-StB, and all ER days (denoted by "All"). The left column shows the amplitudes of potential temperature in Region-P. The middle column shows the amplitudes of wind velocities in Region-S, and the right column shows the amplitudes of the north-south thermal contrast (denoted by "$\Delta\theta$") and EHR amount in Region-C. The thermal contrast is defined as the difference in 925-hPa potential temperature between the northern and southern boundaries of Region-C. Red numbers denote the percentages of average values of type-StB that are greater than those of type-WkB. The markers "O" denote that the anomalies of type-WkB/StB relative to all the ER days are statistically significant at the 0.05 level, while the markers "X" denote the opposite.

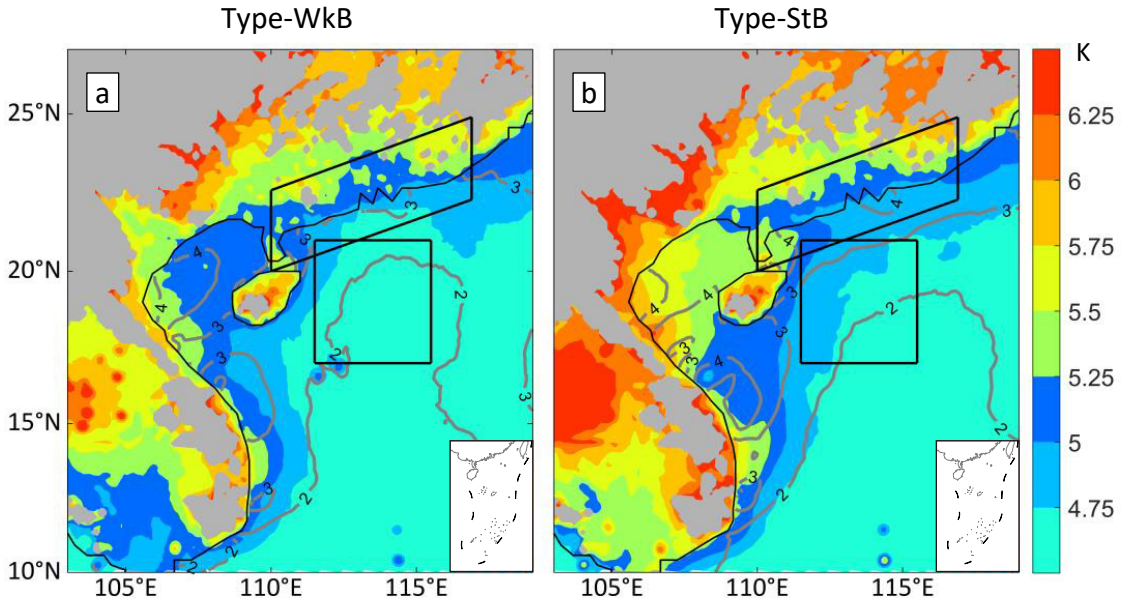



**Fig. 11.** Amplitudes of diurnal variations in potential temperature (shadings) and southerly components (contours; units: m $s^{-1}$) at 950 hPa during (a) type-WkB and (b) type-StB days. The black frames denote the two key regions.

Exp-NoDHTrr, while the EHR amounts at the northern center significantly decrease (Figs. 12b, f, h). The average EHR amounts in Region-C in Exp-NoDH, Exp-NoTrr, and Exp-NoDHTrr are 27.2%, 33%, and 46.7% less than Exp-Ctrl (Figs. 12d, f, h), which are more significant than the changes in total rainfall (Figs. 12c, e, g). This suggests that heavier rainfall is more sensitive to the changes in the Indochina Peninsula.

The cooling over the Indochina Peninsula weakens the MABL southerlies over the northern SCS (Figs. 13a, c). The 950-hPa potential temperatures over the western SCS in sensitivity experiments are 0.5–2 K lower than Exp-Ctrl, leading to a weaker thermal contrast and thus weaker baroclinicity in the MABL. The 950-hPa zonal geopotential gradient in Region-S is weaker in the sensitivity experiments than Exp-Ctrl, which weakens the southerlies. The average 950-hPa southerly components in Region-S decrease by 0.95, 1.25, and 1.36 m $s^{-1}$ in Exp-NoDH, Exp-NoTrr, and Exp-NoDHTrr, respectively (Figs. 13a, c). The impacts of modifying the terrain and diabatic heating are different, since the former has both dynamic and thermodynamic effects. Without the blocking effect of mountains, the southwesterly wind near the Indochina Peninsula is enhanced in Exp-NoTrr, but the cooling over the western SCS weakens the southerlies in Region-S (Fig. 13b). Nevertheless, southerlies over the entire SCS are weakened in Exp-NoDH (Fig. 13a) due to the elimination of diabatic heating. Exp-NoDHTrr features its most significant decrease in southerly components in Region-S, indicating a superposition of terrain and diabatic heating effects. The weakening of southerlies reduces MABL moisture and thus lowers the convective available potential energy (CAPE). The 950-hPa mixing ratio of water vapor is decreased by 0.2–0.5 g $kg^{-1}$ to the southeast of Hainan Island (Figs. 13d, f). The average CAPE in Region-S decreases by 140.4, 166.9, and 320.1 J $kg^{-1}$ in Exp-NoDH, Exp-NoTrr, and Exp-NoDHTrr, respectively (Figs. 13d–f). Note that the changes in terrain in the latter two experiments decrease the consumption of water vapor over the Indochina Peninsula and increase the MABL moisture, which offsets the impacts of cooling and increases the local CAPE (Figs. 13e, f).

The weakened coastal convergence, together with the lower CAPE, inhibits the convection and thus the production of EHR over the SCC. As shown in Fig. 14a, the southerlies near the coastline have a structure typical of a BLJ, with the southerly wind component exceeding 10 m $s^{-1}$ below 900 hPa. The coastal convergence triggers intense convection, which can be seen from the absolute values of vertical velocity. In sensitivity experiments, the southerly wind components near the coastline are decreased by more than 1 m $s^{-1}$ (Figs. 14b–d), which hardly reach 10 m $s^{-1}$. This weakens the convergence in the boundary layer and updraft over the SCC. The absolute values of vertical velocity near the coastline are decreased by 10%–30% in sensitivity experiments (Figs. 14b–d), indicating a substantial weakening of convection.

## 7. Summary

ER events on the SCC involve complex multiscale mechanisms, which makes their prediction very challenging (Sun et al., 2019; Luo et al., 2020). The strong southerlies in the MABL are usually a prerequisite for the production of ER, since they transport warm moist air from the northern SCS and produce coastal convergence through interactions with local factors such as the coastal terrain (Du et al., 2020a;

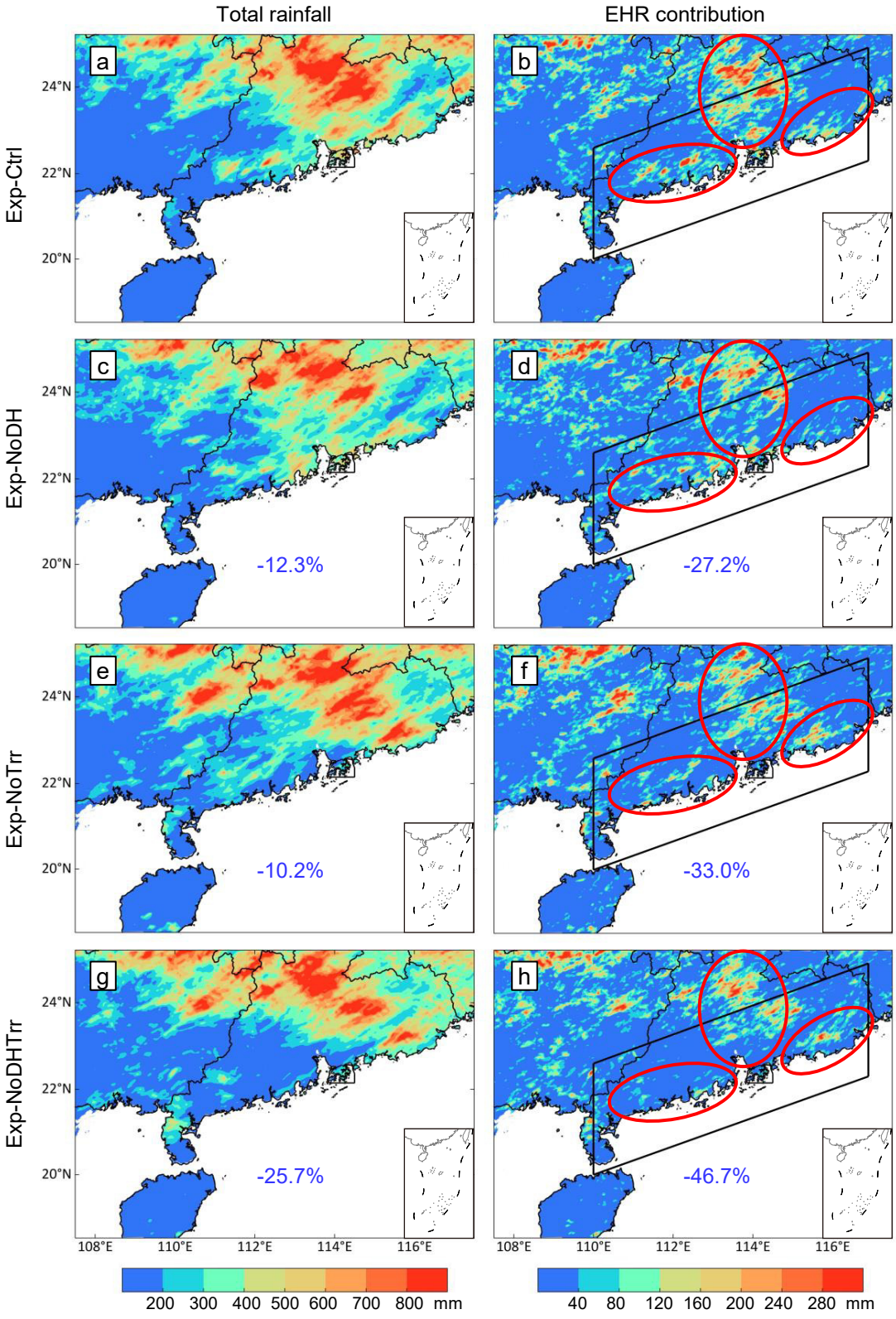



**Fig. 12.** 20-day rainfall amounts (left column) and EHR amounts (right column) during 1–20 June 2022 simulated by different numerical experiments (marked at the left). The numbers in (c–h) represent the changes in the average rainfall amounts in Region-C for sensitivity experiments relative to Exp-Ctrl. Black frames in the right column denote Region-C, and the red ellipses indicate the three areas with the greatest EHR.

Zhang et al., 2022; Su et al., 2023) and land-sea breeze circulations (Chen et al., 2016; Gao et al., 2022; Huang et al., 2024), as well as urban heat island effects (Yin et al., 2020; Sun et al., 2021). Based upon statistical analyses and convec-

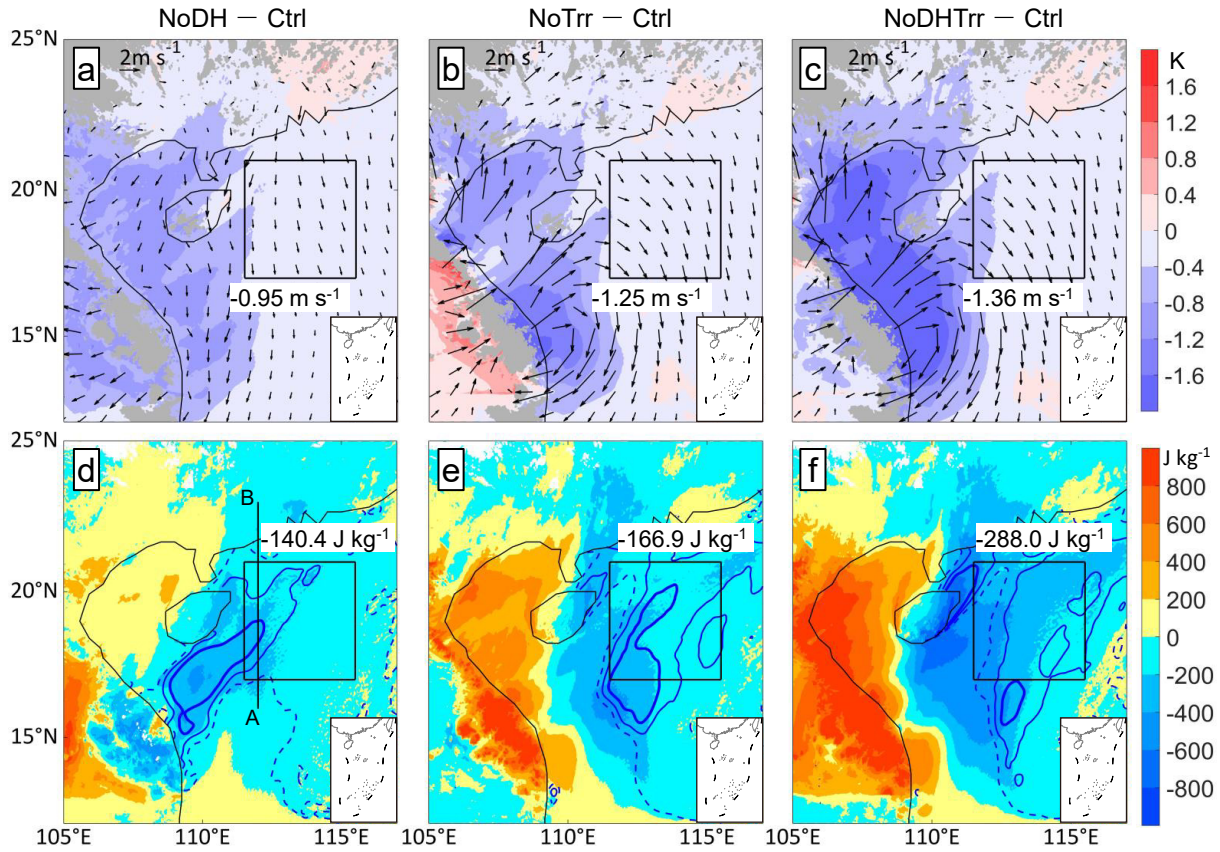



**Fig. 13.** Comparison of thermal structures and wind velocities in the MABL between sensitivity experiments and Exp-Ctrl during 1–20 June 2022. Each column shows the difference between an experiment and Exp-Ctrl (marked at top). The upper row shows the differences in potential temperature (shadings) and wind velocity (vectors) at 950 hPa, and the lower row shows the differences in CAPE (shadings) and mixing ratio of water vapor at 950 hPa (contours). The dashed, thin-solid, and thick-solid lines denote the values of 0, –0.2, and –0.4 g kg$^{-1}$, respectively. Black frames outline Region-S. Line A-B in (d) shows the cross-section referenced in Fig. 14. Black numbers in the upper row and in the lower row denote the average differences of southerly component and CAPE in Region-S, respectively.

tion-permitting numerical simulations, this study proposes a new perspective, in that the Indochina Peninsula, which is located upstream of the northern SCS in the monsoon airflow, augments the southerlies and moisture transport in the MABL through thermodynamic forcing and thus plays an important role in the production of ER on the SCC.

Using the 99th percentile hourly rainfall as the threshold of EHR, 337 days in 30 early summers from 1988 to 2017 are defined as the coastal ER days. Compared to the seasonal average, the coastal ER days feature stronger diabatic heating over the Indochina Peninsula as well as stronger downdrafts over the leeside of the Annamite Range, producing a much warmer MABL over the western SCS and thus enhancing the low-level baroclinicity over the northern SCS. The 950-hPa potential temperature decreases from southwest to northeast over the northern SCS. According to the force analyses, the horizontal thermal contrast dominates the vertical variation in geopotential gradient, which, together with the friction, leads to significant 700–950-hPa VWS. Specifically, the southerly component increases with pressure, while the westerly component decreases with pressure. Thus, the daily average 700–950-hPa VWSs are closely correlated to the daily thermal contrasts. The strengthening of southerlies in the MABL enhances the moisture transport and produces a center of pronounced water vapor convergence over the SCC.

The ER days with strong and weak low-level baroclinicities, which are denoted by the type-StB and type-WkB days, are selected based on the 700–950-hPa VWS for comparative analyses. The 950-hPa potential temperature over the Indochina Peninsula and the western SCS is much warmer during type-StB days than during type-WkB days, further establishing the important role of heating over the peninsula in generating low-level baroclinicity over the northern SCS. The stronger southerlies in the MABL for type-StB produce a stronger gradient of moisture and more precipitable water near the SCC compared to that in type-WkB, thus its coastal ER amount is 37% greater. Moreover, type-StB days feature more drastic diurnal variations in both the MABL wind velocities and the land-sea thermal contrast, thus the amplitude of its diurnal variation for coastal ER is 21% larger than that for type-WkB.

To investigate the impacts of Indochina Peninsula on ER on the SCC, this study conducts a series of numerical sim-

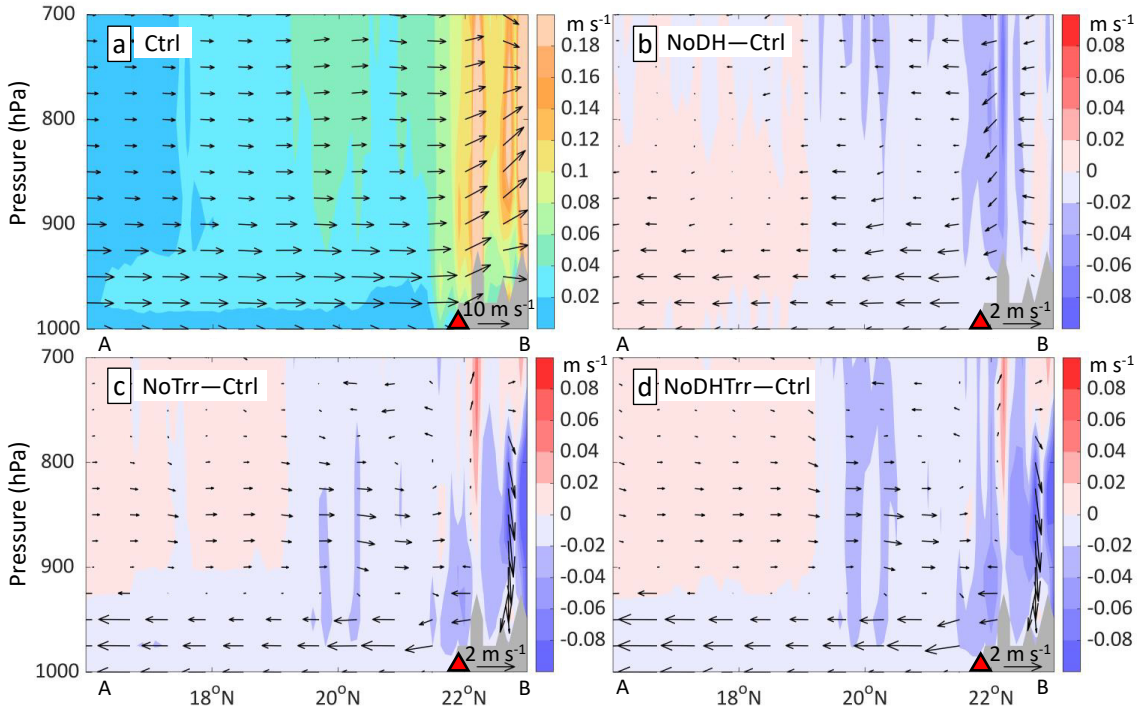



**Fig. 14.** Cross-section along line A-B in Fig. 13d: (a) Absolute values of vertical velocity (shadings) and in-plane wind velocities (vectors; the vertical velocity is multiplied by 50) for Exp-Ctrl; (b) Same as in (a), but for the differences between Exp-NoDH and Exp-Ctrl; (c) Same as in (a), but for the differences between Exp-NoTrr and Exp-Ctrl; (d) Same as in (a), but for the differences between Exp-NoDHTrr and Exp-Ctrl. Red triangles denote the location of the coastline.

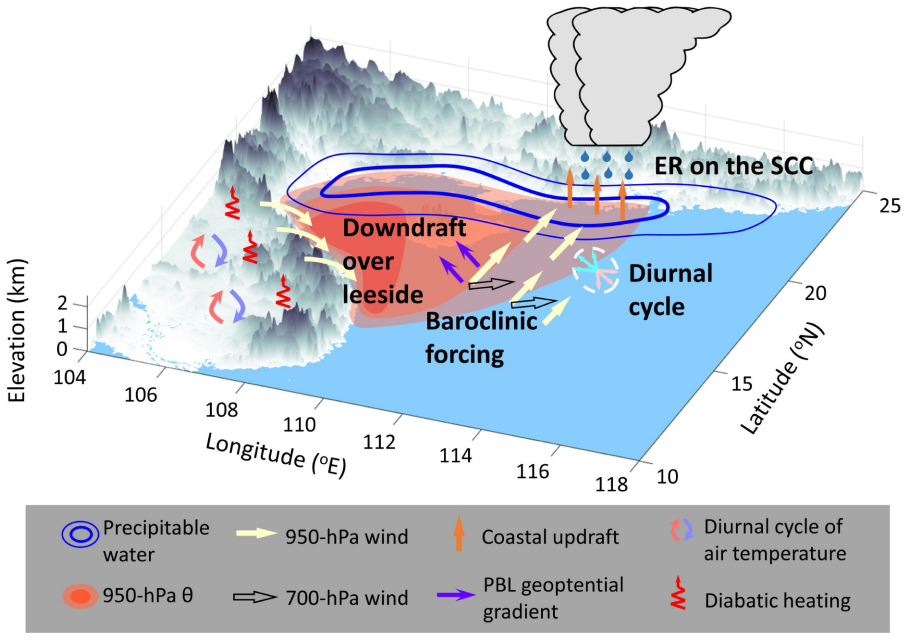



**Fig. 15.** Schematic diagram of how the temperature gradient over the northern South China Sea produced by the upstream heating enhances the MABL southerlies and thus ER on the SCC. See the text for more details.

ulations of a typical heavy rainfall episode during 1–20 June 2022 using the WRF model with a horizontal resolution of 3 km × 3 km. The control experiment well captures the spatiotemporal distribution of ER as well as the low-level thermal structure over the SCC. The sensitivity experiments modifying the terrain or diabatic heating of the eastern Indochina Peninsula can significantly weaken ER on the SCC with decreasing rates ranging from 27.2%–46.7%. The modifica-

tions in sensitivity experiments weaken the heating over the peninsula, leading to a cooler MABL over the western SCS, which significantly weakens the transport of warm moist air in the MABL through thermodynamic forcing. The weakened coastal convergence, together with lower CAPE, inhibits moist convection over the SCC.

According to the above results, the impacts of the Indochina Peninsula can be summarized as follows (Fig. 15). The diabatic heating over the peninsula, together with downdraft-related adiabatic heating over the leeside of the Annamite Range, produces a warm region in the MABL over the western SCS. The southwest warm advection extends its margin to the northern SCS and produces a strong southwestward temperature gradient. Forced by the baroclinicity, the zonal geopotential gradient and southerly component increase with pressure. Thus, the southerlies in MABL are much stronger than in the free atmosphere, which enhances the transport of warm, moist air in the MABL, increasing the precipitable water and CAPE near the SCC. The strengthening of MABL southerlies can also induce the coastal updraft through terrain-induced convergence near the coast. Both impacts are conducive to the production of ER on the SCC. Moreover, the diurnal variation in heating near the peninsula impacts the diurnal variations in the MABL wind and ER on the SCC through thermodynamic forcing.

This study involves regions of several countries, and the results indicate that a better understanding and higher prediction skill of regional extreme weather might be achieved by improving the observation systems through international cooperation. Besides the Indochina Peninsula, Hainan Island also features a notable heating effect upon its surrounding areas (Fig. 3a). The MABL wind can directly bring the warm air from Hainan Island to the SCC, which modulates the coastal thermal structure and rainfall. However, its spatial scale might be quite different from the processes discussed in this paper, and will be analyzed in future work.

***Acknowledgements***. This work was supported by the National Natural Science Foundation of China (Grant Nos. 42205014, U2242203, U2442204), the Basic Research Fund of CAMS (2023Z001), and the State Key Laboratory of Severe Weather Meteorological Science and Technology (2025QZA10).

***Electronic supplementary material***: Supplementary material is available in the online version of this article at https://doi.org/10.1007/s00376-026-5281-8.

***Data availability***. The ERA5 reanalysis data are available from the European Centre for Medium-Range Weather Forecasting (https://cds.climate.copernicus.eu). The EARS reanalysis data and the observation data are hosted on the China Meteorological Administration Data-as-a-Service platform (http://data.cma.cn).

## REFERENCES

Blackadar, A. K., 1957: Boundary layer wind maxima and their significance for the growth of nocturnal inversions. *Bull. Amer. Meteor. Soc.*, **38**, 283–290, https://doi.org/10.1175/1520-0477-38.5.283.

Chakraborty, A., R. S. Nanjundiah, and J. Srinivasan, 2009: Impact of African orography and the Indian summer monsoon on the low-level Somali jet. *International Journal of Climatology*, **29**, 983–992, https://doi.org/10.1002/joc.1720.

Chen, G. X., R. Y. Lan, W. X. Zeng, H. Pan, and W. B. Li, 2018: Diurnal variations of rainfall in surface and satellite observations at the monsoon coast (South China). *J. Climate*, **31**, 1703–1724, https://doi.org/10.1175/JCLI-D-17-0373.1.

Chen, X. C., F. Q. Zhang, and K. Zhao, 2016: Diurnal variations in the land–sea breeze and its related precipitation over South China. *J. Atmos. Sci.*, **73**, 4793–4815, https://doi.org/10.1175/JAS-D-16-0106.1.

Ding, Y. H., 1992: Summer monsoon rainfalls in China. *J. Meteor. Soc. Japan*, **70**, 373–396, https://doi.org/10.2151/jmsj1965.70.1B_373.

Dong, F., X. F. Zhi, L. Zhang, and C. Z. Ye, 2021: Diurnal variations of coastal boundary layer jets over the northern South China Sea and their impacts on diurnal cycle of rainfall over southern China during the early-summer rainy season. *Mon. Wea. Rev.*, **149**, 3341–3363, https://doi.org/10.1175/MWR-D-20-0292.1.

Du, T. R., X. F. Zhi, Y. H. Wang, L. Q. Zhou, L. Zhang, and S. P. Zhu, 2024: The distinct spatial patterns and physical mechanisms of coastal boundary layer jets over the northern South China Sea. *Mon. Wea. Rev.*, **152**, 2639–2660, https://doi.org/10.1175/MWR-D-23-0263.1.

Du, Y., and G. X. Chen, 2019a: Climatology of low-level jets and their impact on rainfall over southern China during the early-summer rainy season. *J. Climate*, **32**, 8813–8833, https://doi.org/10.1175/JCLI-D-19-0306.1.

Du, Y., and G. X. Chen, 2019b: Heavy rainfall associated with double low-level jets over Southern China. Part II: Convection initiation. *Mon. Wea. Rev.*, **147**, 543–565, https://doi.org/10.1175/mwr-d-18-0102.1.

Du, Y., and S. Y. Yi, 2025: The relationship scenarios between boundary layer jet and coastal heavy rainfall during the pre-summer rainy season of South China. *J. Meteor. Res.*, **39**, 26–40, https://doi.org/10.1007/s13351-025-4138-x.

Du, Y., Y.-L. Chen, and Q. H. Zhang, 2015: Numerical simulations of the boundary layer jet off the southeastern coast of China. *Mon. Wea. Rev.*, **143**, 1212–1231, https://doi.org/10.1175/mwr-d-14-00348.1.

Du, Y., Y. A. Shen, and G. X. Chen, 2022: Influence of coastal marine boundary layer jets on rainfall in South China. *Adv. Atmos. Sci.*, **39**, 782–801, https://doi.org/10.1007/s00376-021-1195-7.

Du, Y., G. X. Chen, B. Han, L. Q. Bai, and M. H. Li, 2020a: Convection initiation and growth at the coast of South China. Part II: Effects of the terrain, coastline, and cold pools. *Mon. Wea. Rev.*, **148**, 3871–3892, https://doi.org/10.1175/MWR-D-20-0090.1.

Du, Y., G. X. Chen, B. Han, C. Mai, L. Q. Bai, and M. H. Li, 2020b: Convection initiation and growth at the coast of South China. Part I: Effect of the marine boundary layer jet. *Mon. Wea. Rev.*, **148**, 3847–3869, https://doi.org/10.1175/MWR-D-20-0089.1.

Finnigan, J., and Coauthors, 2020: Boundary-layer flow over complex topography. *Bound.-Layer Meteorol.*, **177**, 247–313, https://doi.org/10.1007/s10546-020-00564-3.

Gao, X. Y., Y. L. Luo, Y. L. Lin, and X. H. Bao, 2022: A source of WRF simulation error for the early - summer warm - sector heavy rainfall over South China coast: Land - sea thermal contrast in the boundary layer. *J. Geophys. Res.: Atmos.*, **127**, e2021JD035179, https://doi.org/10.1029/2021JD035179.

Gao, X. Y., J. S. Sun, J. F. Yin, A. Abulikemu, C. Wu, X. D. Liang, and R. D. Xia, 2024: The impact of mountain-plain thermal contrast on precipitation distributions during the "23·7" record-breaking heavy rainfall over North China. *Atmospheric Research*, **310**, 107582, https://doi.org/10.1016/j.atmosres.2024.107582.

Hersbach, H., and Coauthors, 2020: The ERA5 global reanalysis. *Quart. J. Royal Meteor. Soc.*, **146**, 1999–2049, https://doi.org/10.1002/qj.3803.

Holton, J. R., 1967: The diurnal boundary layer wind oscillation above sloping terrain. *Tellus*, **19**, 199–205, https://doi.org/10.1111/j.2153-3490.1967.tb01473.x.

Hong, S.-Y., Y. Noh, and J. Dudhia, 2006: A new vertical diffusion package with an explicit treatment of entrainment processes. *Mon. Wea. Rev.*, **134**, 2318–2341, https://doi.org/10.1175/mwr3199.1.

Huang, L., L. Q. Bai, and Y. J. Zhang, 2024: Analysis of uncertainties in convection-permitting ensemble simulations of land breeze and nocturnal coastal rainfall in South China. *J. Meteor. Res.*, **38**, 1047–1063, https://doi.org/10.1007/s13351-024-4075-0.

Iacono, M. J., J. S. Delamere, E. J. Mlawer, M. W. Shephard, S. A. Clough, and W. D. Collins, 2008: Radiative forcing by long-lived greenhouse gases: Calculations with the AER radiative transfer models. *J. Geophys. Res.: Atmos.*, **113**, D13103, https://doi.org/10.1029/2008jd009944.

Jiang, Q. F., S. P. Wang, and L. O'Neill, 2010: Some insights into the characteristics and dynamics of the Chilean low-level coastal jet. *Mon. Wea. Rev.*, **138**, 3185–3206, https://doi.org/10.1175/2010MWR3368.1.

Jiang, Z. N., D. L. Zhang, R. D. Xia, and T. T. Qian, 2017: Diurnal variations of presummer rainfall over southern China. *J. Climate*, **30**, 755–773, https://doi.org/10.1175/JCLI-D-15-0666.1.

Kong, H., Q. H. Zhang, Y. Du, and F. Zhang, 2020: Characteristics of coastal low - level jets over Beibu Gulf, China, during the early warm season. *J. Geophys. Res.: Atmos.*, **125**, e2019JD031918, https://doi.org/10.1029/2019JD031918.

Li, J., and Y.-L. Chen, 1998: Barrier jets during TAMEX. *Mon. Wea. Rev.*, **126**, 959–971, https://doi.org/10.1175/1520-0493(1998)126<0959:BJDT>2.0.CO;2.

Li, X. Q., and Y. Du, 2021: Statistical relationships between two types of heavy rainfall and low-level jets in South China. *J. Climate*, **34**, 8549–8566, https://doi.org/10.1175/JCLI-D-21-0121.1.

Li, Z. H., Y. L. Luo, Y. Du, and J. C. L. Chan, 2020: Statistical characteristics of pre-summer rainfall over South China and associated synoptic conditions. *J. Meteor. Soc. Japan*, **98**, 213–233, https://doi.org/10.2151/jmsj.2020-012.

Luo, Y. L., R. D. Xia, and J. C. L. Chan, 2020: Characteristics, physical mechanisms, and prediction of pre-summer rainfall over South China: Research progress during 2008–2019. *J. Meteor. Soc. Japan*, **98**, 19–42, https://doi.org/10.2151/jmsj.2020-002.

Luo, Y. L., M. W. Wu, F. M. Ren, J. Li, and W.-K. Wong, 2016: Synoptic situations of extreme hourly precipitation over China. *J. Climate*, **29**, 8703–8719, https://doi.org/10.1175/jcli-d-16-0057.1.

Luo, Y. L., and Coauthors, 2017: The southern China monsoon rainfall experiment (SCMREX). *Bull. Amer. Meteor. Soc.*, **98**, 999–1013, https://doi.org/10.1175/BAMS-D-15-00235.1.

Shen, Y. A., and Y. Du, 2023: Sensitivity of boundary layer parameterization schemes in a marine boundary layer jet and associated precipitation during a coastal warm-sector heavy rainfall event. *Frontiers in Earth Science*, **10**, 1085136, https://doi.org/10.3389/feart.2022.1085136.

Skamarock, W. C., and Coauthors, 2021: A description of the advanced research WRF model version 4.3.[Available online from https://opensky.ucar.edu/islandora/object/technotes%3A576]

Su, L., J. C. H. Fung, J. L. Li, and W. K. Wong, 2021: Trends in diurnal cycle of summertime rainfall over coastal South China in the past 135 years: Characteristics and possible causes. *J. Geophys. Res.: Atmos.*, **126**, e2020JD033621, https://doi.org/10.1029/2020JD033621.

Su, L., X. Sun, Y. Du, J. C. H. Fung, and G. X. Chen, 2023: The roles of local convergences in the convection initiation of a record - breaking rainfall event at the coastal Pearl River Delta in South China. *J. Geophys. Res.: Atmos.*, **128**, e2022JD037234, https://doi.org/10.1029/2022JD037234.

Su, L., J. H. Hu, Y. Du, J. L. Li, and G. X. Chen, 2025: Boundary-layer and low-level moisture fluxes during low-level jet events in South China and their relationship with early summer rainfall. *J. Climate*, **38**, 1691–1713, https://doi.org/10.1175/JCLI-D-23-0561.1.

Sun, J. H., Y. C. Zhang, R. X. Liu, S. M. Fu, and F. Y. Tian, 2019: A review of research on warm-sector heavy rainfall in China. *Adv. Atmos. Sci.*, **36**, 1299–1307, https://doi.org/10.1007/s00376-019-9021-1.

Sun, X. Y., Y. L. Luo, X. Y. Gao, M. W. Wu, M. X. Li, L. Huang, D.-L. Zhang, and H. M. Xu, 2021: On the localized extreme rainfall over the Great Bay area in South China with complex topography and strong UHI effects. *Mon. Wea. Rev.*, **149**, 2777–2801, https://doi.org/10.1175/MWR-D-21-0004.1.

Tewari, M., and Coauthors, 2004: Implementation and verification of the unified NOAH land surface model in the WRF model. 20th Conf. on Weather Analysis and Forecasting/16th Conf. on Numerical Weather Prediction

Thompson, G., P. R. Field, R. M. Rasmussen, and W. D. Hall, 2008: Explicit forecasts of winter precipitation using an improved bulk microphysics scheme. Part II: Implementation of a new snow parameterization. *Mon. Wea. Rev.*, **136**, 5095–5115, https://doi.org/10.1175/2008mwr2387.1.

Tu, C.-C., Y.-L. Chen, P.-L. Lin, and Y. Du, 2019: Characteristics of the marine boundary layer jet over the South China Sea during the early summer rainy season of Taiwan. *Mon. Wea. Rev.*, **147**, 457–475, https://doi.org/10.1175/MWR-D-18-0230.1.

Wang, X. C., M. Xue, K. F. Zhu, Y. H. Zhang, and Z. Q. Fan, 2022: Diurnal variation of summer monsoon season precipitation over southern Hainan Island, China: The role of boundary layer inertial oscillations over Indochina Peninsula. *J. Geophys. Res.: Atmos.*, **127**, e2022JD037114, https://doi.org/10.1029/2022JD037114.

Westra, S., and Coauthors, 2014: Future changes to the intensity and frequency of short-duration extreme rainfall. *Rev. Geo-*

*phys.*, **52**, 522–555, https://doi.org/10.1002/2014RG000464.

Wu, N. G., X. R. Zhuang, J. Z. Min, and Z. Y. Meng, 2020b: Practical and intrinsic predictability of a warm - sector torrential rainfall event in the South China monsoon region. *J. Geophys. Res.: Atmos.*, **125**, e2019JD031313, https://doi.org/10.1029/2019JD031313.

Wu, N. G., X. Ding, Z. P. Wen, G. X. Chen, Z. Y. Meng, L. X. Lin, and J. Z. Min, 2020a: Contrasting frontal and warm-sector heavy rainfalls over South China during the early-summer rainy season. *Atmospheric Research*, **235**, 104693, https://doi.org/10.1016/j.atmosres.2019.104693.

Xia, F., X. G. Huang, J. F. Fei, J. Wang, X. P. Cheng, and C. Zhang, 2023: Mechanisms of ageostrophic wind convergence in the boundary layer of coastal warm - sector extreme heavy rainfall in South China. *J. Geophys. Res.: Atmos.*, **128**, e2022JD038472, https://doi.org/10.1029/2022JD038472.

Yin, J., and Coauthors, 2023: East Asia Reanalysis System (EARS). *Earth System Science Data*, **15**, 2329–2346, https://doi.org/10.5194/essd-15-2329-2023.

Yin, J. F., D.-L. Zhang, Y. L. Luo, and R. Y. Ma, 2020: On the extreme rainfall event of 7 May 2017 over the coastal city of Guangzhou. Part I: Impacts of urbanization and orography. *Mon. Wea. Rev.*, **148**, 955–979, https://doi.org/10.1175/MWR-D-19-0212.1.

Zeng, Z. L., and D. H. Wang, 2022: Observations of heavy short-term rainfall hotspots associated with warm-sector episodes over coastal South China. *Atmospheric Research*, **276**, 106273, https://doi.org/10.1016/j.atmosres.2022.106273.

Zhang, D.-L., S. L. Zhang, and S. J. Weaver, 2006: Low-level jets over the mid-Atlantic states: Warm-season climatology and a case study. *J. Appl. Meteorol. Climatol.*, **45**, 194–209, https://doi.org/10.1175/JAM2313.1.

Zhang, M. R., and Z. Y. Meng, 2019: Warm-sector heavy rainfall in southern China and its WRF simulation evaluation: A low-level-jet perspective. *Mon. Wea. Rev.*, **147**, 4461–4480, https://doi.org/10.1175/MWR-D-19-0110.1.

Zhang, M. R., K. L. Rasmussen, Z. Y. Meng, and Y. P. Huang, 2022: Impacts of coastal terrain on warm-sector heavy-rain-producing MCSs in Southern China. *Mon. Wea. Rev.*, **150**, 603–624, https://doi.org/10.1175/mwr-d-21-0190.1.

Zhang, R. H., Y. Q. Ni, L. P. Liu, Y. L. Luo, and Y. H. Wang, 2011: South China heavy rainfall experiments (SCHeREX). *J. Meteor. Soc. Japan*, **89A**, 153–166, https://doi.org/10.2151/jmsj.2011-A10.